Performance Analysis of SM-OTFS Under Imperfect Channel Estimation

Halvin Yang, *Member, IEEE,* Sangarapillai Lambotharan, *Senior Member, IEEE*, Mahsa Derakhshani, *Senior Member, IEEE,*, Lajos Hanzo, *Life Fellow, IEEE*

***Abstract*—In this correspondence, we derive closed-form bit error rate (BER) expressions for a Spatial Modulated Orthogonal Time Frequency Space (SM-OTFS) system under imperfect channel state information (CSI). We consider both Zero Forcing (ZF) and Minimum Mean Square Error (MMSE) based equalization techniques. OTFS modulation exhibits robustness against Doppler shifts and multipath fading, while Spatial Modulation (SM) enhances the spectral efficiency by utilizing the antenna index to encode additional information. However, imperfect CSI due to realistic channel estimation errors encountered in rapidly varying channel conditions significantly degrades the system performance. We analyze the effects of imperfect CSI on the BER performance of an SM-OTFS system for different equalization methods and SM orders. The closed-form expressions derived provide valuable insights into the trade-offs between the equalizer type, channel estimation accuracy, and system performance, demonstrating the necessity for robust channel estimation and resilient equalization strategies in high-mobility environments.**

***Index Terms*—Spatial modulation, MIMO, OTFS, SM-OTFS, CSI, CSI error, channel estimation**

I. Introduction

Orthogonal Time Frequency Space (OTFS) modulation has emerged as a Doppler-resilient alternative to traditional multi-carrier modulation schemes in wireless communication. It is particularly well suited for doubly selective fading environments, such as the high-mobility scenarios of next-generation (NG) networks [1]. By transforming information symbols from the time-frequency domain into the delay-Doppler (DD) domain, OTFS effectively mitigates the inter-symbol interference (ISI) and inter-carrier interference (ICI) caused by time-frequency selectivity [2]. Recent advances have also explored OTFS for integrated sensing and communications (ISAC) applications and high-mobility environments, where accurate delay–Doppler parameter estimation and beamforming are critical [3].

Spatial Modulation (SM), able to improve spectral efficiency at reduced complexity, beneficially complements OTFS by leveraging spatial diversity without requiring multiple radio frequency chains [4], [5]. In an SM-OTFS system, the information is jointly mapped across the time, frequency, and spatial domains, allowing for robust communication under challenging propagation conditions. However, these benefits are significantly impacted by the accuracy of channel state information (CSI) in real-world deployments [6].

Halvin Yang is with the Department of Electrical and Electronic Engineering, Imperial College London, UK (email: halvin.yang@imperial.ac.uk)

Sangarapillai Lambotharan is with the Institute for Digital Technologies, Loughborough University London, Loughborough University, London, UK (email: s.lambotharan@lboro.ac.uk)

Mahsa Derakhshani is with the Wolfson School of Mechanical Electrical and Manufacturing Engineering at Loughborough University, Loughborough, U.K. (e-mail: M.Derakhshani@lboro.ac.uk).

Lajos Hanzo is with the School of Electronics and Computer Science, University of Southampton, Southampton, UK (email: lh@ecs.soton.ac.uk)

The financial support of the following Engineering and Physical Sciences Research Council (EPSRC) projects is gratefully acknowledged: Platform for Driving Ultimate Connectivity (TITAN) (EP/X04047X/1; EP/Y037243/1); Robust and Reliable Quantum Computing (RoaRQ, EP/W032635/1); PerCom (EP/X012301/1); India-UK Intelligent Spectrum Innovation ICON UKRI-1859

	[1]	[8]	[11]	[12]	[13]	[9]	our work
OTFS	✓	✓	✓	✓	✓		✓
Spatial Modulation					✓	✓	✓
CSI Error		✓	✓			✓	✓
Zero Forcing Equalisation			✓	✓			✓
MMSE Equalisation				✓			✓

TABLE I: Positioning of this correspondence relative to the prior art.

Accurate CSI is critical in SM-OTFS systems, especially when employing minimum mean square error (MMSE) equalization, which relies on precise channel estimates for counteracting delay-Doppler impairments encountered [7]. The impact of channel estimation errors in pure OTFS schemes has been explored in [8], but no prior works have addressed the unique challenges that arise when realistic imperfect CSI is used in SM-OTFS systems. Consequently, there is a pressing need for quantifying the impact of CSI imperfections in SM-OTFS, where estimation errors could degrade the system's resilience to fading and Doppler effects, ultimately affecting its reliability and throughput [9].

This correspondence addresses the open problem of analysing SM-OTFS under imperfect CSI. While previous works have studied OTFS with estimation errors [8] and SM-OTFS under ideal CSI [13], the joint impact of CSI inaccuracies on SM-OTFS with closed-form BER analysis for linear equalizers has not been reported. In contrast to OTFS-only studies that overlook antenna-index detection, and SM-only studies with CSI errors [9] that ignore delay–Doppler coupling and OTFS equalisation, we derive and validate closed-form BER expressions for SM-OTFS under ZF and MMSE detection. Our analysis quantifies BER degradation due to imperfect CSI and provides insights into designing more robust SM-OTFS systems for high-mobility next-generation scenarios, with contributions summarised in Table I. Similar analytical frameworks have recently been extended to non-terrestrial links [10], further demonstrating the relevance of imperfect-CSI analysis for high-mobility channels.

This correspondence is organised as follows. Section II presents our transceiver architecture and our system model. Section III explores how ZF and MMSE equalisation will be implemented and derives the corresponding BER expressions. Section IV presents our results, comparing the performance of both equalisation as well as the impact of channel estimation error followed by conclusions in Section V. The notation and definitions used in this paper are defined in II.

II. Transceiver Architecture

A. Modulation and Mapping

A specific bit-to-symbol mapping is required in order to implement spatial modulation as well as the classic quadrature amplitude modulation (QAM). This subsection will describe how the whole OTFS frame can be characterised according to this joint modulation scheme, as seen in Figure 1.

Let N_t and N_r represent the number of transmit antennas (TA) and receive antennas (RA) respectively. In this MIMO

Symbol	Meaning
S, Q	Number of subcarriers/time slots per OTFS frame
T, Δf	Symbol duration ($T{=}1/\Delta f$), subcarrier spacing
T_{frame}	Frame duration ($T_{\text{frame}}{=}QT$)
N_t, N_r	# transmit/receive antennas
M	QAM order; bits per QAM symbol $= \log_2 M$
L_{SM}, L_{QAM}	Bits via SM / QAM ($\log_2 N_t$, $\log_2 M$)
B	Bandwidth ($B = S\Delta f$)
$\mathbf{X}_{DD}$, $\mathbf{Y}_{DD}$	Transmit / receive DD-domain vectors/matrices
$\mathbf{H}_{\text{DD}}$	Stacked DD-domain channel (all RAs/TAs)
$\mathbf{H}^{DD}_{n_r,n_t}$	Per-link DD channel (RA n_r, TA n_t)
ρ^2	CSI accuracy
σ_η^2	AWGN variance
$\mathrm{E_b/N_0}$	Energy-per-bit to noise-density ratio

TABLE II: Main notation used throughout the paper.

system, they are moving at high speeds, which warrants the usage of OTFS to offset the detrimental effects on the signal. By defining the number of subcarriers and the number of time slots of an OTFS frame as S and Q respectively, the bandwidth of the OTFS signal can be defined as $B = S\Delta f$, where Δf is the subcarrier spacing, and the frame duration is $T_{\text{frame}} = QT$ where T is the symbol duration. With the characteristics of the OTFS frame now established, the modulation process can be defined. Since there are S subcarriers and Q time slots, there are a total of SQ different slots available for the data to be transmitted in. Therefore an input bit stream $\mathbf{b}$ of length L_b would be split into groups, each with $\frac{L_b}{SQ}$ bits. Then, $\mathbf{b}$ can be defined as $\mathbf{b} = [\mathbf{b}_1, \mathbf{b}_2, ..., \mathbf{b}_{SQ-1}, \mathbf{b}_{SQ}]$.

The bits in $\mathbf{b}_{sq}$th group, i.e., bits being transmitted by the sth subcarrier at the qth time slot, are mapped both to the TA SM and QAM conventional symbols. This bit group is further separated into $\mathbf{b}^{\text{SM}}_{sq}$ and $\mathbf{b}^{\text{QAM}}_{sq}$ which represent the mapping into the spatial and phase-amplitude domains. The number of bits conveyed by SM can be defined as $L_{\text{SM}} = \log_2 N_t$, which is also the length of $\mathbf{b}^{\text{SM}}_{sq}$. Likewise, the number of bits carried by QAM of order M (M-QAM) can be defined as $L_{\text{QAM}} = \log_2 M$, which is the length of $\mathbf{b}^{\text{QAM}}_{sq}$. Therefore, the total length of the bit stream to be transmitted per frame is:

$$L_b = SQ(L_{\text{SM}} + L_{\text{QAM}}) = SQ\log_2(MN_t). \tag{1}$$

There are SQ groups of data that have to be transmitted in the OTFS frame, using a single TA at any given transmission instance in order to perform spatial modulation. The OTFS frame $\mathbf{F} \in \mathbb{C}^{N_t \times SQ}$ can now be defined as:

$$\mathbf{F} = \begin{bmatrix} F(0,0) & \dots & F(0, SQ-1) \\ \vdots & \ddots & \vdots \\ F(N_t-1, 0) & \dots & F(N_t-1, SQ-1) \end{bmatrix}, \tag{2}$$

where each column represents a transmission instance with a single nonzero term for the active TA, while each row corresponds to a different TA.

B. Transmitter

After obtaining the overall OTFS frame in (2), this matrix has to be transformed into the time domain for transmission. First, the transmission matrix of each antenna is extracted from $\mathbf{F}$. The transmission matrix for the n_tth TA in the delay-doppler domain can then be defined as:

$$\mathbf{X}_{n_t} = \text{vec}^{-1}(\mathbf{F}^{\text{T}}_{n_t}), \tag{3}$$

where $\mathbf{F}_{n_t}$ is the n_tth row of matrix $\mathbf{F}$ and $\text{vec}^{-1}(\cdot)$ is the inverse vectorisation operator. To find the time-domain signal, $\mathbf{X}_{n_t}$ is first transformed into the time-frequency domain using the inverse symplectic Fourier transform (ISFFT) [1]:

$$\bar{X}_{n_t}(sq) = \frac{1}{\sqrt{SQ}} \sum_{a=1}^{S} \sum_{b=1}^{Q} X_{n_t}(a,b) e^{j2\pi\left(\frac{qb}{Q} - \frac{sa}{S}\right)}. \tag{4}$$

Given $\bar{X}_{n_t}(sq)$, using a Heisenberg transform [1], [2], the time domain signal transmitted by the n_tth TA can be formulated as

$$s_{n_t}(t) = \sum_{s=1}^{S} \sum_{q=1}^{Q} \bar{X}_{n_t}(sq) g_{\text{tpulse}}(t - qT) e^{-j2\pi s\Delta f(t-qT)}, \tag{5}$$

where $g_{\text{tpulse}}(t - qT)$ is the transmit pulse at the qth time slot and $\bar{X}_{n_t}(sq)$ is the element located at sq in the time-frequency domain transmission matrix $\bar{\mathbf{X}}_{n_t}$.

C. Channel

We consider an imperfect time-varying non-line-of-sight (nLOS) fading channel. The channel between the n_tth transmitter and n_rth receiver having a total of P paths and a channel estimation accuracy of ρ can be expressed as

$$h_{n_r,n_t}(\tau,\nu) = \sum_{i=1}^{P} \left(\rho h_{i,n_r,n_t} + \sqrt{1-\rho^2}\,\Delta h_{i,n_r,n_t}\right) \times \delta(\tau - \tau_i)\delta(\nu - \nu_i), \tag{6}$$

where $\tau_i = \frac{\bar{\tau}_i}{B}$ and $\nu_i = \frac{\bar{\nu}_i}{T_f}$ are the delay and Doppler indices aligned with the OTFS grid, $h_{i,n_r,n_t} \sim \mathcal{CN}(0, d_{\text{tr}}^{-\zeta}/P)$ is the true complex gain of the ith path with d_{tr} denoting the distance between the transmitter and receiver and ζ representing the path-loss exponent, and $\Delta h_{i,n_r,n_t} \sim \mathcal{CN}(0, d_{\text{tr}}^{-\zeta})$ is the i.i.d. estimation error. The coefficient $\rho \in [0,1]$ is the correlation between the true and estimated path gains, so ρ^2 quantifies the CSI accuracy. Perfect CSI is recovered when $\rho = 1$.

Definition 1. *The CSI accuracy is quantified by the squared correlation between the true and estimated path gains:*

$$\rho \triangleq \frac{\mathbb{E}[h\hat{h}^*]}{\sqrt{\mathbb{E}|h|^2\,\mathbb{E}|\hat{h}|^2}}, \qquad \rho^2 \in [0,1].$$

Here $\rho^2 = 1$ denotes perfect CSI, while $\rho^2 = 0$ corresponds to a completely uncorrelated estimate.

Remark 1. *For analytical tractability, we assume that all path delays and Doppler shifts are aligned with the OTFS grid, so that each path contributes to a single (τ_i, ν_i) bin as in (6). In practice, fractional Doppler results in inter-bin leakage and additional interference, which would tighten BER at low–moderate SNR. A rigorous treatment of fractional Doppler is left for future work.*

D. Receiver

The signal at the n_rth RA from the n_tth TA can be expressed as:

$$r_{n_r,n_t}(t) = \iint \hat{h}_{n_r,n_t}(\tau,\nu)\, s_{n_t}(t-\tau)\, e^{j2\pi\nu(t-\tau)}\, d\tau d\nu + \eta_{n_r,n_t}(t), \tag{7}$$

where $\eta_{n_r,n_t}(t) \sim \mathcal{CN}(0, \sigma_\eta^2)$ is the complex additive white Gaussian noise (AWGN). To obtain the received signal matrix in

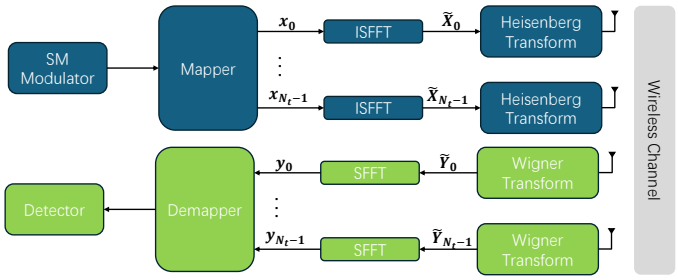

Fig. 1: Transceiver architecture of SM-OTFS.

DD domain, first, (7) is converted to the time-frequency domain using the Wigner transform:

$$\bar{Y}_{n_r,n_t}(s,q) = \int r_{n_r,n_t}(t) g_{rx}(t-qT) e^{j2\pi s\Delta f(t-qT)} dt. \quad (8)$$

Then, by applying the SFFT, (9) can be obtained. The received signal matrix in the delay-Doppler domain is $\mathbf{Y}_{n_r,n_t}$. The $\tilde{s},\tilde{q}$th element of this matrix can be expressed as:

$$Y_{n_r,n_t}(\tilde{s},\tilde{q}) = \sum_{s=1}^{S}\sum_{q=1}^{Q} \frac{\bar{Y}_{n_r,n_t}(s,q)}{\sqrt{SQ}} e^{-j2\pi\left(\frac{\tilde{q}q}{Q}-\frac{\tilde{s}s}{S}\right)}, \quad (9)$$

where $\tilde{s}=1,...,S$ and $\tilde{q}=1,...,Q$. Similar to the transmitter process, the signal received at n_rth RA can be expressed as

$$\mathbf{y}_{n_r} = \sum_{n_t=0}^{N_t-1} \mathrm{vec}(\mathbf{Y}_{n_r,n_t}). \quad (10)$$

Finally, by stacking $\mathbf{y}_{n_r}$, the received signal matrix can be obtained as $\mathbf{Y}_{DD} = [\mathbf{y}_0^{\mathrm{T}},...,\mathbf{y}_{N_r-1}^{\mathrm{T}}]^{\mathrm{T}}$. Having acquired the received signal matrix in the delay Doppler domain, equalisation can be used for recovering the original data.

Lemma 1. *Under white Gaussian noise $\eta(t)\sim\mathcal{CN}(0,\sigma_\eta^2)$ and unit-energy pulses, the TF and DD-domain noises remain white with the same variance: $\mathbf{W}_{TF}\sim\mathcal{CN}(\mathbf{0},\sigma_\eta^2\mathbf{I})$ and $\mathbf{W}_{DD}\sim\mathcal{CN}(\mathbf{0},\sigma_\eta^2\mathbf{I})$.*

Proof: The TF samples are inner products of $r(t)$ with orthonormal time-frequency shifts of $g_{rx}(\cdot)$; under the unit-energy assumption, the mapping from time to TF is unitary. The subsequent SFFT from TF to DD is also unitary up to the $1/\sqrt{SQ}$ scaling already included in (9). For a unitary matrix $\mathbf{U}$ and $\mathbf{w}\sim\mathcal{CN}(\mathbf{0},\sigma_\eta^2\mathbf{I})$, we have $\mathbf{Uw}\sim\mathcal{CN}(\mathbf{0},\sigma_\eta^2\mathbf{I})$. Hence the variance is preserved through TF and DD transforms. ■

III. Equalisation

This section will cover both ZF and MMSE equalisation. First, we need to obtain the channel matrix in the delay-Doppler domain which is contaminated by the estimation error.

Lemma 2 (DD channel sampling)**.** *Given (6), the DD channel matrix between the n_rth RA and n_tth TA, $\mathbf{H}_{n_r,n_t}^{DD}$, is formulated as:*

$$\mathbf{H}_{n_r,n_t}^{DD}(k,l) = \sum_{i=1}^{P}\left(\rho h_{i,n_r,n_t} + \sqrt{1-\rho^2}\,\Delta h_i^{n_r,n_t}\right)\delta_{k,k_i}\delta_{l,l_i}, \quad (11)$$

where $\delta_{k,k_i},\delta_{l,l_i}$ are Kronecker delta functions to ensure that each path i only contributes to its own corresponding delay–Doppler bin.

Proof: To represent the channel in the DD domain, the channel response is first sampled on a discrete DD grid. The delay and Doppler bins can be expressed as $\tau = k\Delta\tau$ and $\nu = l\Delta\nu$, respectively, where $k=0,1,...,S-1$, $l=0,1,...,Q-1$, $\Delta\tau=\frac{1}{B}$ and $\Delta\nu=\frac{1}{T_f}$ are the delay and Doppler resolutions. The objective is to create a discrete DD channel matrix $\mathbf{H}_{n_r,n_t}^{DD}$, where each element, $H_{n_r,n_t}^{DD}(k,l)$, represents the channel response at that specific DD bin (k,l).

Observing (6), each path i is mapped onto its corresponding DD bins (k_i,l_i) by finding the closest points on the DD grid:

$$k_i = \mathrm{round}\left(\frac{\tau_i}{\Delta\tau}\right), \qquad l_i = \mathrm{round}\left(\frac{\nu_i}{\Delta\nu}\right), \quad (12)$$

where round$(\cdot)$ rounds to the nearest integer. Then, the contribution of the ith path is added to its corresponding grid location. For the ith path the matrix element $\mathbf{H}_{n_r,n_t}^{DD}(k_i,l_i)$ is:

$$\mathbf{H}_{n_r,n_t}^{DD}(k_i,l_i) \leftarrow \mathbf{H}_{n_r,n_t}^{DD}(k_i,l_i) + \left(\rho h_{i,n_r,n_t} + \sqrt{1-\rho^2}\,\Delta h_i^{n_r,n_t}\right). \quad (13)$$

After summing all the paths in (13), we have $\mathbf{H}_{n_r,n_t}^{DD}(k,l) = \sum_{i=1}^{P}\mathbf{H}_{n_r,n_t}^{DD}(k_i,l_i)$, which establishes (11). This result characterises the sampled DD channel only; the residual error matrix used later arises after left-multiplying by $\mathbf{H}_{DD}^{-1}$ and inserting the estimation discrepancy $\hat{\mathbf{H}}_{DD}-\mathbf{H}_{DD}$. ■

Therefore, the overall DD channel matrix can be written as $\mathbf{H}_{DD} = [(\sum_{n_t=0}^{N_t-1}\mathrm{vec}(\mathbf{H}_{1,n_t}^{DD}))^{\mathrm{T}},...,(\sum_{n_t=0}^{N_t-1}\mathrm{vec}(\mathbf{H}_{N_r-1,n_t}^{DD}))^{\mathrm{T}}]^{\mathrm{T}}$.

A. Zero Forcing Equalisation

ZF equalisation attempts to remove the effect of the channel by multiplying the received signal matrix by the inverse of the perceived channel matrix, yielding:

$$\tilde{\mathbf{X}}_{DD} = \mathbf{H}_{DD}^{-1}\mathbf{Y}_{DD} = \mathbf{H}_{DD}^{-1}\hat{\mathbf{H}}_{DD}\mathbf{X}_{DD} + \mathbf{H}_{DD}^{-1}\mathbf{W}_{DD} \quad (14)$$

However, since the perceived channel matrix has estimation error, we have $\mathbf{H}_{DD}\neq\hat{\mathbf{H}}_{DD}$ and therefore ZF fails to perfectly cancel out the impact of the channel; consequently, the inter-symbol interference is not completely eliminated.

Since $\hat{\mathbf{H}}_{DD}\neq\mathbf{H}_{DD}$ under imperfect CSI, we may write $\mathbf{H}_{DD}^{-1}\hat{\mathbf{H}}_{DD} = \mathbf{I}+\mathbf{E}_{DD}$, $\mathbf{E}_{DD}\triangleq\mathbf{H}_{DD}^{-1}(\hat{\mathbf{H}}_{DD}-\mathbf{H}_{DD})$, which motivates the residual interference term $\mathbf{E}_{DD}$ used below.

Lemma 3. *With $\mathbf{E}_{DD}=\mathbf{H}_{DD}^{-1}(\hat{\mathbf{H}}_{DD}-\mathbf{H}_{DD})$ and independent, zero-mean estimation errors whose entries have variance $(1-\rho^2)$ after DD-domain normalization,*

$$\mathbb{E}\left[\|\mathbf{E}_{DD}\mathbf{X}_{DD}\|^2\right] \approx (1-\rho^2)\,\|\mathbf{H}_{DD}^{-1}\|^2\,\mathbb{E}\left[\|\mathbf{X}_{DD}\|^2\right]. \quad (15)$$

Proof: Let $\Delta=\hat{\mathbf{H}}_{DD}-\mathbf{H}_{DD}$ and $\mathbf{A}=\mathbf{H}_{DD}^{-1}$, so $\mathbf{E}_{DD}\mathbf{X}_{DD}=\mathbf{A}\Delta\mathbf{X}_{DD}$. The matrix Δ has i.i.d. entries $\mathcal{CN}(0,1-\rho^2)$ and is independent of $\mathbf{X}_{DD}$. By isotropy of i.i.d. Gaussian matrices, for any fixed $\mathbf{A}$ and any $\mathbf{Z}$ independent of Δ, $\mathbb{E}[\|\mathbf{A}\Delta\mathbf{Z}\|_F^2]=(1-\rho^2)\|\mathbf{A}\|_F^2\,\mathbb{E}[\|\mathbf{Z}\|_F^2]$. With $\mathbf{Z}=\mathbf{X}_{DD}$ we obtain (15). ■

Theorem 1. *The BER for ZF equalisation relying on imperfect channel estimation can be expressed as*

$$BER_{ZF} \approx \frac{2}{\log_2 M}\left(1-\frac{1}{\sqrt{M}}\right) \times \mathrm{Q}\left(\sqrt{\frac{3E_s}{(M-1)\left(\mathbb{E}\left[\|\mathbf{E}_{DD}\mathbf{X}_{DD}\|^2\right]+\sigma_\eta^2\,\|\mathbf{H}_{DD}^{-1}\|^2\right)}}\right). \quad (16)$$

Proof: In order to calculate the BER, the signal to interference plus noise ratio (SINR) has to be obtained first. Due to imperfect CSI, there is an extra interference term as well as the noise. The SINR can be approximated as

$$\text{SINR}_{\text{ZF}} = \frac{\mathbb{E}[||\mathbf{X}_{DD}||^2]}{\mathbb{E}[||\mathbf{E}_{DD}\mathbf{X}_{DD}||^2] + \text{Var}(\mathbf{H}_{DD}^{-1}\mathbf{W}_{DD})}, \tag{17}$$

where $\mathbb{E}[||\mathbf{E}_{DD}\mathbf{X}_{DD}||^2]$ represents the power of the interference term due to channel estimation errors and $\text{Var}(\mathbf{H}_{DD}^{-1}\mathbf{W}_{DD}) = \sigma_\eta^2||\mathbf{H}_{DD}^{-1}||^2$ is the variance of the amplified noise. Since the BER of M-QAM is commonly approximated as [14]

$$\text{BER}_{\text{QAM}} \approx \frac{2}{\log_2 M}\left(1 - \frac{1}{\sqrt{M}}\right)\text{Q}\left(\sqrt{\frac{3\,\text{SINR}}{M-1}}\right), \tag{18}$$

substituting (17) into (18) completes the proof. ∎

Lemma 4. *The BER expression of ZF equalisation under imperfect channel estimation can be simplified as*

$$BER_{ZF} \approx \frac{2}{\log_2 M}\left(1 - \frac{1}{\sqrt{M}}\right) \times \text{Q}\left(\sqrt{\frac{3}{(M-1)\left\|\mathbf{H}_{DD}^{-1}\right\|^2\left((1-\rho^2) + \sigma_\eta^2/E_s\right)}}\right). \tag{19}$$

Proof: By Lemma 3,

$$\mathbb{E}[||\mathbf{E}_{DD}\mathbf{X}_{DD}||^2] \approx (1-\rho^2)\,||\mathbf{H}_{DD}^{-1}||^2\,\mathbb{E}[||\mathbf{X}_{DD}||^2]. \tag{20}$$

Substituting (20) into (17) yields

$$\text{SINR}_{\text{ZF}} \approx \frac{1}{||\mathbf{H}_{DD}^{-1}||^2\left((1-\rho^2) + \frac{\sigma_\eta^2}{\mathbb{E}[||\mathbf{X}_{DD}||^2]}\right)}. \tag{21}$$

Finally, substitute (21) into (18) to obtain (19). ∎

B. MMSE Equalisation

Before MMSE equalisation is implemented, the DD channel at the n_rth RA is given by:

$$Y_{n_r} = \rho\hat{H}_{n_r,n_t}X_{n_t} + \sqrt{1-\rho^2}\,\Delta H_{n_r,n_t}X_{n_t} + W_{n_r}, \tag{22}$$

where $\hat{H}_{n_r,n_t}$ is the channel coefficient between the n_tth TA and n_rth RA, $\Delta H_{n_r,n_t}$ is the estimation error (zero-mean complex Gaussian with variance σ_h^2) and W_{n_r} is the AWGN at the n_rth RA with variance σ_η^2.

MMSE equalisation aims for estimating the transmitted symbol by minimizing the mean squared error between the estimated symbol and the actual transmitted symbol. The MMSE equaliser for the n_rth RA is derived for minimizing:

$$\text{MMSE} = \mathbb{E}\left[|X_{n_t} - \hat{X}_{n_t}|^2\right], \tag{23}$$

where $\hat{X}_{n_t}$ is the estimate of X_{n_t} obtained from $\hat{X}_{n_t} = G_{n_r}Y_{n_r}$ with G_{n_r} the MMSE equalisation coefficient.

Theorem 2. *The MMSE equalisation coefficient for the n_rth RA is:*

$$G_{n_r} = \frac{\rho\hat{H}_{n_r,n_t}}{\rho^2|\hat{H}_{n_r,n_t}|^2 + (1-\rho^2)\sigma_h^2 + \sigma_\eta^2}. \tag{24}$$

Proof: Refer to Appendix A. ∎

Parameter	Value / Assumption
Frame size (S, Q)	$(64, 16)$
Subcarrier spacing Δf	$15\,\text{kHz}$ $\quad(T = 1/\Delta f)$
Bandwidth B	$S\Delta f = 960\,\text{kHz}$
Transmit/Receive antennas (N_t, N_r)	$(4, 4)$ unless varied)
QAM order M	4 (QPSK) unless varied
Paths P & delay support	$P = 4$ taps within $[0, (P-1)\Delta\tau]$
Max Doppler	$\nu_{\max} = 200$ Hz (integer bins)
Pathloss exponent	$\zeta = 3.5$ (normalized distance)
Noise variance	set via $\text{E}_\text{b}/\text{N}_0$ sweep
Time variations	constant within frame, i.i.d. across frames
CSI accuracy	$\rho^2 \in [0, 1]$; error var. $(1-\rho^2)$

TABLE III: Simulation parameters (used unless otherwise noted).

Lemma 5. *The estimated transmitted symbol $\hat{X}_{n_t}$ is obtained by applying the MMSE equaliser to the received signal:*

$$\hat{X}_{n_t} = \frac{\rho^2|\hat{H}_{n_r,n_t}|^2}{D}X_{n_t} + \frac{\rho\hat{H}_{n_r,n_t}}{D}\sqrt{1-\rho^2}\,\Delta H_{n_r,n_t}X_{n_t} + \frac{\rho\hat{H}_{n_r,n_t}}{D}W_{n_r}, \tag{25}$$

where $D = \rho^2|\hat{H}_{n_r,n_t}|^2 + (1-\rho^2)\sigma_h^2 + \sigma_\eta^2$.

Proof: (25) follows by substituting (22) and (24) into $\hat{X}_{n_t} = G_{n_r}Y_{n_r}$. ∎

Lemma 6. *The SINR of MMSE equalisation can be expressed as:*

$$SINR_{MMSE} = \frac{\rho^2|\hat{H}_{n_r,n_t}|^2}{(1-\rho^2)\sigma_h^2 + \sigma_\eta^2}. \tag{26}$$

Proof: Rewrite (25) as $\hat{X}_{n_t} = \frac{\rho^2|\hat{H}_{n_r,n_t}|^2}{D}X_{n_t} + N_{\text{eff}}$, where $N_{\text{eff}} = \frac{\rho\hat{H}_{n_r,n_t}}{D}\left(\sqrt{1-\rho^2}\,\Delta H_{n_r,n_t}X_{n_t} + W_{n_r}\right)$ is the effective noise after equalisation. Taking second moments yields (26). ∎

Theorem 3. *The BER of MMSE equalisation can be expressed for imperfect channel estimation as*

$$BER_{MMSE} = \left(\frac{\log_2(N_t)(N_t-1)}{2\log_2(N_tM)N_t} + \frac{2(\sqrt{M}-1)}{\log_2(N_tM)\sqrt{M}}\right) \times \left(1 - \sqrt{\frac{\rho^2}{(1-\rho^2) + \frac{d_{tr}^\zeta}{SNR}}}\right), \tag{27}$$

where $SNR = \frac{E_b}{N_0B}$, d_{tr} is the distance between the transmitter and receiver, and ζ is the pathloss exponent.

Proof: Refer to Appendix B. ∎

Observed from the BER expression of MMSE equalisation, the BER is affected by the transmission power, pathloss, channel estimation accuracy and the modulation orders.

IV. Numerical Results

Unless otherwise stated, the parameters in Table III are used. The channels obey a Rayleigh distribution with P grid-aligned taps; Doppler shifts are integer-valued on the OTFS grid; taps are constant over one OTFS frame and vary i.i.d. across frames. Estimation error variance is $(1-\rho^2)$ as per Sec. II-C..

Figure 2 compares the numerical and simulation results to verify their accuracy over the considered SNR range. The chosen range already captures the key BER behaviour: the divergence between ZF and MMSE under imperfect CSI and the relative advantage of MMSE at higher CSI accuracies. Upon increasing SNR, the analytical and simulated curves naturally converge since the closed-form expressions are derived from

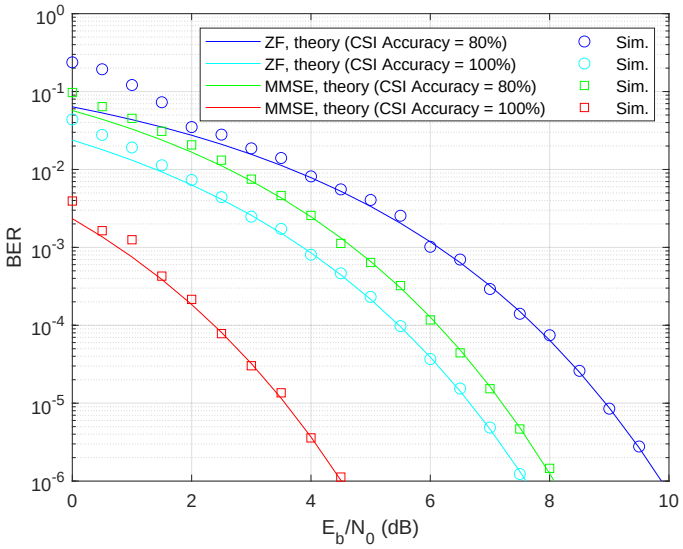

Fig. 2: Comparison of the numerical and simulated BER of both ZF and MMSE equalisation under perfect and imperfect CSI.

high-SNR approximations and rely on Gaussian-distributed interference terms that remain accurate under the studied setup. In this scenario, 4 TAs are used for SM with 4-QAM, and $N_r = 4$ receive antennas. The close agreement observed above approximately 2 dB arises because the Q-function-based BER expressions provide a tight fit once the system operates beyond the noise-dominant region. At low SNR, however, small discrepancies emerge as the assumptions of Gaussianity and interference dominance no longer hold strictly, causing the analytical approximation to slightly underestimate the simulated BER. Nevertheless, the overall trends and relative performance differences between ZF and MMSE are well captured, confirming the validity of the derived expressions.

Figure 3 further investigates the impact of CSI accuracy on BER. There are $N_t = 4$ TAs and 4-QAM is considered, as well as $\frac{E_b}{N_0} = 2$ dB. As expected, for higher CSI accuracy the ZF and MMSE equalization techniques are more accurate. There are two interesting points of note: at low CSI accuracies the BER of ZF and MMSE seem to converge; at high CSI accuracies MMSE significantly outperforms ZF.

This can be explained by the inherent design of both equalizers. ZF aims for completely eliminating interference between the different signals transmitted, while MMSE uses the CSI to calculate a weight matrix that minimizes the overall mean square error by balancing the noise and interference reduction. ZF is designed for completely eliminating interference at the cost of potential noise enhancement. At low CSI accuracy, both ZF and MMSE become heavily affected by channel imperfections. ZF suffers from unreliable channel inversion leading to noise amplification, while MMSE loses its ability to optimally balance noise and interference. The result is that their BERs converge because the key strength of MMSE to balance interference and noise becomes ineffective when the channel estimate is highly inaccurate, while ZF also struggles due to noise amplification.

As the CSI accuracy increases, ZF does a better job of eliminating interference, but it still lacks a potent strategy to control noise, which limits the BER improvement. On the other hand, MMSE optimally combines the received signals for minimizing the combined impact of both noise and interference. As the CSI improves, MMSE becomes more efficient at obtaining a

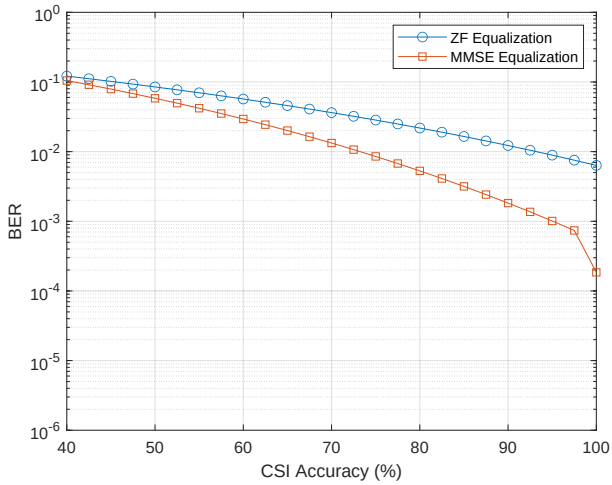

Fig. 3: Impact of CSI accuracy (ρ^2) on BER at $\mathrm{E_b/N_0} = 2$ dB.

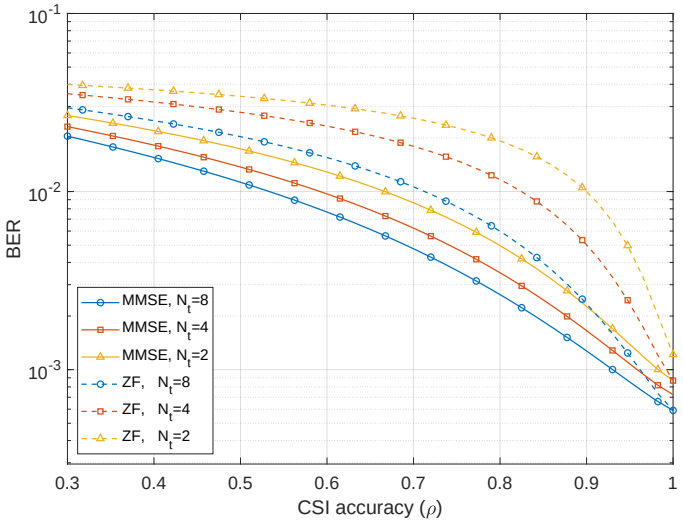

Fig. 4: BER versus CSI accuracy ρ^2 at $\mathrm{E_b/N_0} = 2$ dB for $N_t \in \{2, 4, 8\}$ and M=4, comparing ZF and MMSE equalisation.

balance in minimizing the total error. This leads to a better BER reduction compared to ZF, that focuses only on interference without explicitly addressing the effect of noise.

Fig. 4 illustrates the impact of transmit antennas and equalisation schemes on CSI robustness. The BER versus ρ^2 is shown at $\mathrm{E_b/N_0} = 2$ dB for $N_t \in \{2, 4, 8\}$ with M=4. As N_t increases, antenna-index detection becomes more sensitive to estimation errors, and BER degrades more rapidly with decreasing ρ^2. This is because (i) the set of possible antenna indices expands, (ii) per-antenna channels must be estimated more accurately, and (iii) index errors directly cause symbol errors. Furthermore, MMSE equalisation consistently outperforms ZF, as it mitigates noise enhancement and is more robust to imperfect CSI, while ZF exhibits stronger degradation as ρ^2 decreases.

Remark 2. *Including fractional Doppler (off-grid ν_i) is expected to further degrade the BER due to inter-bin leakage and additional interference. A rigorous treatment with leakage-aware detection is left for future work, while the current model assumes grid-aligned Doppler for analytical tractability.*

V. Conclusion

In conclusion, we investigated the impact of imperfect CSI on the performance of SM integrated with OTFS modulation. Our results demonstrate a significant difference in BER

when considering CSI errors, highlighting the importance of accounting for channel imperfections in SM-OTFS systems. Future work should continue to explore strategies to mitigate the effects of imperfect CSI, ensuring more robust and reliable communication in SM-OTFS systems. Additionally, the analysis in this paper underscores the need for advanced estimation and compensation techniques to handle CSI imperfections. By considering various levels of channel inaccuracies, our study provides a more comprehensive understanding of their influence on system reliability and efficiency. To the best of our knowledge, this is the first correspondence to provide closed-form BER expressions for SM-OTFS under imperfect CSI with both ZF and MMSE equalization. Future work will explicitly incorporate fractional Doppler (to quantify leakage-induced interference in finite grids), extend the analysis to more realistic channels such as the 3GPP EVA profile, and explore ML-based channel estimation/prediction to enhance CSI quality for high-mobility SM-OTFS links.

Appendix A
Derivation of MMSE Equaliser Coefficient

To find G_{n_r}, first MMSE needs to be computed and its derivative with respect to G_{n_r} set to zero.

$$\text{MMSE} = \mathbb{E}\left[|X_{n_t} - G_{n_r} Y_{n_r}|^2\right]. \tag{28}$$

Looking at (22), Y_{n_r} can be rewritten as $Y_{n_r} = \rho \hat{H}_{n_r,n_t} X_{n_t} + W_{eff}$, where $W_{eff} = \sqrt{1-\rho^2}\,\Delta H_{n_r,n_t} X_{n_t} + W_{n_r}$ is the effective noise, including the interference imposed by the channel estimation error. W_{eff} has zero mean and a variance of σ^2_{eff}:

$$\sigma^2_{eff} = (1-\rho^2)\sigma^2_h + \sigma^2_\eta, \tag{29}$$

assuming that $\mathbb{E}\left[|X_{n_t}|^2\right] = 1$. Now the MMSE expression in (28) can be rewritten in terms of W_{eff} as:

$$\text{MMSE} = \mathbb{E}\left[\left|\left(1 - G_{n_r}\rho \hat{H}_{n_r,n_t}\right) X_{n_t} - G_{n_r} W_{eff}\right|^2\right]. \tag{30}$$

Since X_{n_t} and W_{eff} are independent and X_{n_t} has zero mean and unit variance, the expectation expands to

$$\text{MMSE} = \left|1 - G_{n_r}\rho \hat{H}_{n_r,n_t}\right|^2 + |G_{n_r}|^2 \sigma^2_{eff}. \tag{31}$$

Differentiating MMSE with respect to G_{n_r} and setting it to zero, the MMSE equaliser is

$$G_{n_r} = \frac{\rho \hat{H}_{n_r,n_t}}{\rho^2 |\hat{H}_{n_r,n_t}|^2 + \sigma^2_{eff}} = \frac{\rho \hat{H}_{n_r,n_t}}{\rho^2 |\hat{H}_{n_r,n_t}|^2 + (1-\rho^2)\sigma^2_h + \sigma^2_\eta}, \tag{32}$$

which matches (24).

Appendix B
Derivation of the BER of the MMSE Equaliser

The overall BER can be formulated as a weighted sum of the BER of SM and the BER of QAM, relying on the number of bits allocated to each modulation scheme, yielding:

$$\text{BER}_{\text{MMSE}} = \frac{1}{\log_2(N_t M)}\left(\log_2(N_t)\,\text{BER}_{\text{SM}} + \log_2(M)\,\text{BER}_{\text{QAM}}\right). \tag{33}$$

Lemma 7. *The BER for SM can be approximated as:*

$$BER_{SM} \approx \frac{1}{2}\left(1 - \frac{1}{N_t}\right)\left(1 - \sqrt{\frac{SINR_{MMSE}}{1 + SINR_{MMSE}}}\right). \tag{34}$$

Proof: The probability of incorrectly detecting the active TA is derived using the union bound and pairwise error probability in Rayleigh fading channels. The factor $(1 - \frac{1}{N_t})$ is the probability that the incorrect TA is chosen out of $N_t - 1$ possibilities. ∎

Lemma 8. *The BER for QAM can be approximated as:*

$$BER_{QAM} \approx \frac{2}{\log_2(M)}\left(1 - \frac{1}{\sqrt{M}}\right)\left(1 - \sqrt{\frac{SINR_{MMSE}}{1 + SINR_{MMSE}}}\right). \tag{35}$$

Proof: This approximation is popularly used in BER calculations for M-QAM over Rayleigh fading channels, where the BER is a function of SINR. ∎

By substituting (26) into (35) and (34) and substituting these expressions into (33), the final expression for the overall BER can be obtained.

References

[1] Z. Wei *et al.*, "Orthogonal Time-Frequency Space Modulation: A Promising Next-Generation Waveform," *IEEE Wireless Commun.*, vol. 28, no. 4, pp. 136-144, Aug. 2021.

[2] S. Li, J. Yuan, W. Yuan, Z. Wei, B. Bai, and D. W. K. Ng, "Performance Analysis of Coded OTFS Systems Over High-Mobility Channels," *IEEE Trans. Wireless Commun.*, vol. 20, no. 9, pp. 6033-6048, Sept. 2021.

[3] B. Jin, X. Lu, X. Luo, Y. Wang, H. H. Yang, and K. Yang, "Super-Resolution Parameter Estimation and Predictable Beamforming Optimization for MIMO-OTFS ISAC Systems," *IEEE Trans. Veh. Technol.*, doi: 10.1109/TVT.2025.3596241.

[4] R. Y. Mesleh, H. Haas, S. Sinanovic, C. W. Ahn, and S. Yun, "Spatial Modulation," *IEEE Trans. Veh. Technol.*, vol. 57, no. 4, pp. 2228-2241, July 2008.

[5] M. Di Renzo, H. Haas, A. Ghrayeb, S. Sugiura, and L. Hanzo, "Spatial Modulation for Generalized MIMO: Challenges, Opportunities, and Implementation," *Proc. IEEE*, vol. 102, no. 1, pp. 56-103, Jan. 2014.

[6] P. Garg, R. K. Mallik, and H. M. Gupta, "Performance Analysis of Space-Time Coding With Imperfect Channel Estimation," *IEEE Trans. Wireless Commun.*, vol. 4, no. 1, pp. 257-265, Jan. 2005.

[7] D. Zhou *et al.*, "OTFS-Based Robust MMSE Precoding Design in Over-the-Air Computation," *IEEE Trans. Veh. Technol.*, vol. 73, no. 9, pp. 13932-13937, Sept. 2024.

[8] Y. Yue, J. Shi, Z. Li, J. Hu, and Z. Tie, "Model-Driven Deep Learning Assisted Detector for OTFS With Channel Estimation Error," *IEEE Commun. Lett.*, vol. 28, no. 4, pp. 842-846, Apr. 2024.

[9] X. Qian *et al.*, "The Impact of Imperfect CSI on Spatial Modulation Schemes," *IEEE Commun. Lett.*, vol. 24, no. 1, pp. 65-69, 2020.

[10] H. Yang, M. Derakhshani, S. Lambotharan, and L. Hanzo, "Performance Analysis of Fluid Antenna System Aided OTFS Satellite Communications," *IEEE J. Sel. Areas Commun.*, doi: 10.1109/JSAC.2025.3615566.

[11] P. Singh, K. Yadav, H. B. Mishra, and R. Budhiraja, "BER Analysis for OTFS Zero Forcing Receiver," *IEEE Trans. Commun.*, vol. 70, no. 4, pp. 2281-2297, Apr. 2022.

[12] G. D. Surabhi and A. Chockalingam, "Low-Complexity Linear Equalization for 2×2 MIMO-OTFS Signals," in *Proc. IEEE 21st Int. Workshop Signal Process. Adv. Wireless Commun. (SPAWC)*, Atlanta, GA, USA, May 2020, pp. 1-5.

[13] Z. Sui, H. Zhang, Y. Xin, T. Bao, L.-L. Yang, and L. Hanzo, "Low Complexity Detection of Spatial Modulation Aided OTFS in Doubly-Selective Channels," *IEEE Trans. Veh. Technol.*, vol. 72, no. 10, pp. 13746-13751, Oct. 2023.

[14] M.-S. Alouini and M. K. Simon, *Digital Communication over Fading Channels*, 2nd ed. Hoboken, NJ, USA: Wiley, 2005.